

Many-body dissipative particle dynamics simulation of liquid/vapor and liquid/solid interactions

Marco Arienti,^{1,a)} Wenxiao Pan,² Xiaoyi Li,³ and George Karniadakis⁴

¹Sandia National Laboratories, Livermore, California 94550, USA

²Pacific Northwest National Laboratory, Richland, Washington 99352, USA

³United Technologies Research Center, East Hartford, Connecticut 06108, USA

⁴Brown University, Providence, Rhode Island 02912, USA

(Received 2 February 2011; accepted 25 April 2011; published online 27 May 2011)

The combination of short-range repulsive and long-range attractive forces in many-body dissipative particle dynamics (MDPD) is examined at a vapor/liquid and liquid/solid interface. Based on the radial distribution of the virial pressure in a drop at equilibrium, a systematic study is carried out to characterize the sensitivity of the surface tension coefficient with respect to the inter-particle interaction parameters. For the first time, the approximately cubic dependence of the surface tension coefficient on the bulk density of the fluid is evidenced. In capillary flow, MDPD solutions are shown to satisfy the condition on the wavelength of an axial disturbance leading to the pinch-off of a cylindrical liquid thread; correctly, no pinch-off occurs below the cutoff wavelength. Moreover, in an example that illustrates the cascade of fluid dynamics behaviors from potential to inertial-viscous to stochastic flow, the dynamics of the jet radius is consistent with the power law predictions of asymptotic analysis. To model interaction with a solid wall, MDPD is augmented by a set of bell-shaped weight functions; hydrophilic and hydrophobic behaviors, including the occurrence of slip in the latter, are reproduced using a modification in the weight function that avoids particle clustering. The dynamics of droplets entering an inverted Y-shaped fracture junction is shown to be correctly captured in simulations parametrized by the Bond number, confirming the flexibility of MDPD in modeling interface-dominated flows. © 2011 American Institute of Physics. [doi:10.1063/1.3590376]

I. INTRODUCTION

The advantage of dissipative particle dynamics (DPD) resides in the simplicity of the underlying algorithm of particle interaction under a soft repulsive potential. It has been shown that DPD can be constructed as a mesoscopic model of molecular dynamics (MD),¹ where the coarse-graining of Lennard-Jones clusters can lead to a suitable DPD force field. This result holds at sufficient low densities and for small ranges of gyration, when many-body effects can be neglected.

DPD has been used to investigate phase separation in immiscible binary liquid mixtures,^{2–4} droplet deformation and rupture in shear flow,⁵ and droplets on surfaces under the influence of shear flow.⁶ In single-species fluid problems, however, the standard DPD method presents a fundamental limitation, in that the repulsive soft potential alone cannot reproduce surface tension. This potential leads to a predominantly quadratic pressure-density equation of state (EOS),⁷ while a higher-order pressure-density curve is necessary for the coexistence of the liquid and vapor phases.

The free energy of the DPD system was modified by Tiwary and Abraham⁸ to include a correction directly derived from the van der Waals EOS. The new term added the long-range attractive force that is responsible for surface tension between the liquid and the vapor phase; surface tension emerges from the asymmetry of the intermolecular forces acting on a layer of molecules at the liquid-vapor interface. As

this asymmetry causes larger intermolecular distances in the outer layer than in the liquid bulk, the forces in the layer act to contract the interface.

The many-body DPD (MDPD) method by Pagonabarraga and Frenkel⁹ also included an attractive force. The amplitude of the soft repulsion was made proportional to the local density of the particles, thus achieving a cubic pressure-density relation. A similar approach was introduced by Nugent and Posch in the context of smoothed particle hydrodynamics (SPH).¹⁰ The connection between MDPD and SPH was then clarified by Español and Revenga,¹¹ who introduced a smoothed DPD (SDPD) method as a SPH variant based on a new formalism developed for discrete hydrodynamics.¹²

MDPD was extensively investigated by Warren¹³ and Trofimov *et al.*¹⁴ The method can be used for the study of single species free-surface flow, for instance, in the case of pinch-off of a liquid thread during the formation of a drop. There, the vanishing liquid thread diameter induces a singularity in the hydrodynamic description of a two-phase flow interface that is at odds with the continuum description of surface tension as a taut membrane of zero thickness. MDPD can also be used to study free-surface dynamics on solid surfaces; for instance, the microscale physics of slippage. However, the focus of past research has been mostly on bulk properties, namely, the pressure-density relation.¹³ This work focuses instead on the interfacial behavior of the MDPD fluid, on the sensitivity of the surface tension coefficient σ to the particle interaction parameters, and on the comparison with the properties of real liquids.

^{a)}Electronic mail: marient@sandia.gov.

In the following, after outlining the workings of MDPD, an extensive set of simulations is presented for a liquid with number density ρ in coexistence with a very dilute vapor. The dependence of σ from ρ is investigated based on a table of representative interaction parameters. An approximate mean-field expression is derived to directly evaluate the surface tension coefficient from the interaction parameters. The simulation of liquid thread pinch-off is then verified using analysis results derived in the limit of a slender jet. In the second part of this work, the MDPD scheme is combined with a wall interaction model to reproduce static wetting at different contact angles. Slip lengths are calculated for non-wetting liquid-solid interfaces in the case of a driven flow in rectangular 2D channels, and simulations with droplets entering an inverted Y-shaped fracture junction are compared to the experimentally observed behavior.

All the simulations are enabled by the particle dynamics software code LAMMPS (Large-scale Atomic/Molecular Massively Parallel Simulator)¹⁵ with the addition of a new MDPD class. The computationally scalable implementation of LAMMPS guarantees the optimization of the particle interaction calculation through an efficient neighbor list algorithm, and will not be discussed in this work.

II. MDPD SCHEME

MDPD inherits the three pairwise-additive inter-particle forces formulation of the standard DPD scheme, $\mathbf{F}_i = \sum_{i \neq j} \mathbf{F}_{ij}^C + \mathbf{F}_{ij}^D + \Delta t^{-1/2} \mathbf{F}_{ij}^R$, with Δt the simulation time step. The conservative, dissipative, and random forces of this expression are defined, respectively, as

$$\mathbf{F}_{ij}^C = F_{ij}^C(r_{ij}) \hat{\mathbf{r}}_{ij}, \quad (1)$$

$$\mathbf{F}_{ij}^D = -\gamma \omega_D(r_{ij})(\mathbf{v}_{ij} \cdot \hat{\mathbf{r}}_{ij}) \hat{\mathbf{r}}_{ij}, \quad (2)$$

$$\mathbf{F}_{ij}^R = \xi \theta_{ij} \omega_R(r_{ij}) \hat{\mathbf{f}}_{ij}, \quad (3)$$

where $\hat{\mathbf{r}}_{ij} = \mathbf{r}_{ij}/r_{ij}$ and $\mathbf{v}_{ij} = \mathbf{v}_i - \mathbf{v}_j$.

Warren's approach¹³ is pursued for \mathbf{F}_{ij}^C ; the repulsive force depends on a weighted average of the local density, whereas the attractive force is density-independent,

$$F_{ij}^C = A_{ij} w_c(r_{ij}) + B_{ij}(\bar{\rho}_i + \bar{\rho}_j) w_d(r_{ij}). \quad (4)$$

The weight functions $w_c(r) = (1 - r/r_c)$ and $w_d(r) = (1 - r/r_d)$ vanish for $r > r_c$ and $r > r_d$, respectively. Since a DPD method with a single range may not have a stable interface,⁹ in Eq. (4) the repulsive contribution is set to act at a shorter range $r_d < r_c$ than the soft pair attractive potential.

The many-body repulsion is chosen in the form of a self-energy per particle which is quadratic in the local density, $B_{ij}(\bar{\rho}_i + \bar{\rho}_j) w_d(r_{ij})$, where $B > 0$. The density for each particle is defined as

$$\bar{\rho}_i = \sum_{j \neq i} w_\rho(r_{ij}), \quad (5)$$

and its weight function w_ρ is defined as

$$w_\rho(r) = \frac{15}{2\pi r^3} (1 - r/r_d)^2. \quad (6)$$

w_ρ vanishes for $r > r_d$ and for convenience is normalized so that $\int d^3\mathbf{r} w_\rho(r) = 1$.

The DPD thermostat consists of random and dissipative forces. The θ_{ij} coefficients from Eq. (3) are independent identically distributed Gaussian random numbers with zero mean and unit variance. The equilibrium temperature T is maintained through the condition posed by the fluctuation-dissipation theorem

$$w_D(r) = [\omega_R(r)]^2, \quad (7)$$

$$\xi^2 = 2\gamma k_B T, \quad (8)$$

where k_B is the Boltzmann constant. The weight function for the dissipative force is

$$w_D(r) = (1 - r/r_c)^2. \quad (9)$$

Details about the choice of the random and dissipative coefficients ξ and γ can be found in Ref. 16. All the simulations presented in this work are carried out with the velocity Verlet algorithm of Groot and Warren¹⁶ using the value 0.5 for the empirical parameter.

A. MDPD units and coarse-graining

Conventionally, dissipative particle dynamics methods operate in reduced units, such that energy is measured in units of $k_B T$; length in units of r_c , and mass in units of mass of a single particle, m . In the following sections, we will find it convenient to refer to dimensionless quantities such as the Ohnesorge number and the Bond number. Here, however, it is instructive to look at the balance of the physical units of length (L_{DPD}), mass (M_{DPD}), and time (T_{DPD}) in relation to a specific set of properties of a real liquid.

Let us consider the interaction parameters $A = -40$, $B = 40$, $r_d = 0.75$. This set corresponds to entry 2 in Table I, which lists the interaction parameters of the MDPD fluids considered in this study. The number density and the surface tension coefficient can be calculated with simple numerical tests. Details of one methodology will be discussed later; we find $\rho = 5.12$ and $\sigma = 4.69$. The bulk mass density d has the same value in reduced units as the number density, i.e., $d = 5.12$. Viscosity can be assessed separately from ρ and σ , for instance, in a test where a doubly periodic Poiseuille

TABLE I. Parameter sets and properties of MDPD fluids. The bulk density ρ and the surface tension coefficient σ are calculated for $k_B T = 1$.

Set	A	B	r_d	ρ	σ	σ^{fit}
1	-40	40	0.80	3.94	1.90	3.33
2	-40	40	0.75	5.12	4.69	5.63
3	-30	25	0.75	5.27	3.51	4.48
4	-40	80	0.70	5.47	6.89	6.36
5	-50	40	0.75	5.60	8.42	8.43
6	-30	20	0.75	5.80	4.48	5.44
7	-40	25	0.75	6.10	7.30	8.02
8	-40	40	0.70	6.51	10.2	9.11
9	-40	20	0.75	6.77	9.14	9.90
10	-40	25	0.70	7.82	14.7	13.2

(DPP) flow is established; the description of this convenient procedure for creating two opposite Poiseuille flows can be found in Ref. 1. We find that the choice of the values $\gamma = 0.5$ and $\xi = 1$ determines the kinematic viscosity $\nu = 0.472$.

If the same properties of surface tension coefficient, density, and viscosity are expressed in physical units and labeled with an asterisk, dimensional analysis yields to

$$M_{DPD} = L_{DPD}^3 \frac{d^*}{d}, \quad (10)$$

$$T_{DPD} = \left(M_{DPD} \frac{\sigma}{\sigma^*} \right)^{0.5}, \quad (11)$$

$$\frac{L_{DPD}^2}{T_{DPD}} = \frac{\nu^*}{\nu}. \quad (12)$$

According to this system of equations, the properties of water at ambient conditions ($d = 998 \text{ kg/m}^3$, $\sigma = 0.0720 \text{ N/m}$, and $\nu = 1.00 \times 10^{-6} \text{ m/s}^2$) are matched by $M_{DPD} = 3.70 \times 10^{-20} \text{ kg}$, $T_{DPD} = 1.55 \times 10^{-9} \text{ s}$, and $L_{DPD} = 5.75 \times 10^{-8} \text{ m}$. The number of molecules per MDPD particle can now be obtained directly from M_{DPD} divided by the mass of a water molecule; it is $n = 1.24 \times 10^6$.

A different choice of MDPD parameters would lead to different units for the same physical liquid. If we decide that L_{DPD} needs to be doubled, then, according to the previous relations, the unit of mass increases by 8 and the unit of time by $2\sqrt{2}$. The kinematic viscosity of the MDPD fluid now has to be smaller by a factor $\sqrt{2}$, and this requires a different choice of the parameters ξ and γ . Viscosity cannot be arbitrarily decreased, however, as $\nu(\gamma)$ has a minimum with respect to γ .¹⁷ Also, we note that other properties, such as the non-dimensional isothermal compressibility $\kappa^{-1} = (\partial P / \partial \rho)_T / k_B T$, will not generally coincide. For Set 2, $\kappa^{-1} \simeq 50$, whereas for water $\kappa^{-1} = 16$. Thus, matching the surface tension coefficient, density, and kinematic viscosity of a liquid will in general lead to different interaction parameters than the ones obtained by imposing equal compressibility.

Once the physical units have been established, it is important to verify that the fluid dynamic behavior of a system of particles is sufficiently well represented by the coarse-graining level of choice. It can be shown that MDPD is scale-free under a scaling that preserves the physical quantities of interest by following the same approach proposed for DPD by Füchslin.¹⁸ As outlined in the following, this approach requires the modification of the interaction parameters as a function of the coarse-graining level.

Let us consider a system whose particle number N has been scaled by a factor ϕ while keeping the domain size constant. Denoting with a prime the new equivalent system, so that $N' = N/\phi$ and $m' = m\phi$, the scaling relations proposed by Füchslin for three dimensions are $r'_c = r_c \phi^{1/3}$ and $t' = t \phi^{1/3}$. The first relation maintains the fractional particle overlap independent from the coarse-graining level, while the second ensures that velocity increments calculated during one time step are the same for the two systems. For the same argument, the scaled force parameters are

$$A' = A \phi^{2/3}, \quad (13)$$

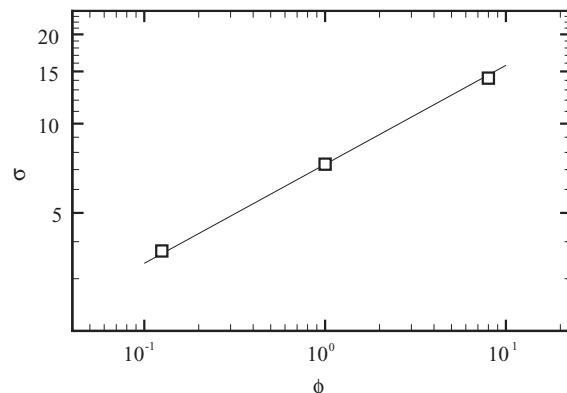


FIG. 1. Variation of the surface tension coefficient under scaling by a factor ϕ .

$$\gamma' = \gamma \phi^{2/3}, \quad (14)$$

$$\xi' = \xi \phi^{5/6}. \quad (15)$$

By construction, the kinematic viscosity ν scales like $\phi^{1/3}$. This means that for an increased coarse-graining $N'/N > 1$ (so that $\phi < 1$), the viscosity $\nu' = \nu \phi^{1/3}$ decreases following the new values of γ' and ξ' . We easily extend the same procedure to MDPD by adding the primed parameters

$$r'_d = r_d \phi^{1/3}, \quad (16)$$

$$B' = B \phi^{5/3}. \quad (17)$$

Following the relations above, scale independence holds for bulk interactions because the energy associated with an individual MDPD particle is made proportional to the number of molecules it represents. However, surface-dependent interaction parameters may be expected to vary with the level of coarse-graining, and in particular we find (by dimensional analysis) that σ must scale with $\phi^{1/3}$.

The dependence of the surface tension coefficient from the level of coarse-graining is illustrated in Fig. 1, where a reference line of slope 1/3 is drawn in the log-log plot of σ with respect to ϕ . The line passes by the point at $\phi = 1$, with the values $\rho = 6.10$ and $\sigma = 7.30$ from the parameter set 7 on Table I. Moving from left to right in the plot corresponds to coarsening the MDPD representation, that is, the interaction parameters become larger as $\phi > 1$. The open symbols in the plot at $\phi = 0.125$ and $\phi = 8$ are obtained by modifying the interaction parameters according to the relations above and by recalculating ρ and σ from MDPD simulations. These points fall very close to the reference line, confirming that, if the number of molecules per particle is changed while keeping fixed the physical dimensions of the domain, Füchslin's scaling relations maintain the fluid density but also change the surface tension coefficient. Fortunately, the surface tension component of the stress tensor varies as σ'/r'_c , or $\phi^{1-1/3-2/3} = \phi^0$, and it is therefore invariant to changes in coarse-graining level. This result will be illustrated in Sec. III B by a convergence study of capillary pinch-off.

III. LIQUID-VAPOR INTERFACE

The operational expression to calculate surface tension at liquid-vapor equilibrium uses the macroscopic normal and tangential pressure values, or, alternatively, a perturbation formalism where surface tension is expressed as the energy difference between a reference state and a state with an infinitesimal area variation. Reference 19 compares the thermodynamic and mechanical routes for MDPD. We examine here the simplified relation that is established between the pressure difference ΔP across the liquid-vapor interface and the shape of a capillary surface according to the Young-Laplace equation (Y-L),

$$\Delta P = \sigma \left(\frac{1}{R_1} + \frac{1}{R_2} \right). \quad (18)$$

In this expression, R_1 and R_2 are the principal radii of curvature of the surface. The Y-L relation is deduced from mechanical stability, and it has been shown to hold even for nanometer-size bubbles.²⁰ The internal pressure of a liquid can be calculated from

$$p^{virial} = \frac{\rho}{3} \langle (\mathbf{v} - \bar{\mathbf{v}})^2 \rangle + \frac{1}{6V} \left\langle \sum_{i \neq j} (\mathbf{r}_i - \mathbf{r}_j) \cdot \mathbf{F}_{i,j}^c \right\rangle, \quad (19)$$

where $\langle \rangle$ denotes the sample average of the particles contained in the volume V and $\bar{\mathbf{v}}$ is the sample velocity after being spatially averaged on V . The first term on the right-end side of Eq. (19) represents the thermal agitation of the molecules of the system. The second term is due to the interaction potential.

By way of illustration, drops with different diameters are simulated from an initial spherical lattice of particles in a box with periodic boundary conditions. The size of the box ensures that the drop is isolated. The initial random velocity distribution is at $k_B T = 1$. This value is maintained in the simulation by fixing the parameters $\xi = 1$ and $\gamma = 0.5$. The virial pressure at equilibrium is plotted in Fig. 2 as a function of radius for the set $A = -40$, $B = 25$, $r_c = 1$, $r_d = 0.80$. In this exercise there is no change in coarse-graining when the droplet radius is varied from one simulation to the next.

The individual plots from Fig. 2 are obtained by taking concentric sampling shells of constant thickness centered at the center of mass of the drop. The center of mass is recalculated at every iteration. Sampling starts at iteration 150 000 (to wash out equilibration transients) and ends at iteration 500 000. Each line represents an average taken over 50 000 time steps. Due to the small number of particles contained in the innermost shells, values near the drop center are strongly affected by noise.

In examining the diagram in Fig. 2(a), it is apparent that the thermal contribution of the virial pressure is constant over most of the drop and that the plateau value is $\rho k_B T$ (the number density is 4.76). At the liquid-vapor surface, the thermal contribution decreases to zero within approximately one unit length. It can be shown that the actual extent of this transition region depends on the temperature of the drop and becomes larger at higher temperatures. The conservative term in Fig. 2(b) has a more complex behavior. Past the fluctuations near the droplet center, this term reaches a constant value when the number of sampled particles becomes sufficiently large.

The negative dip at the drop surface can be attributed to the strengthening of the attractive force as outward layer particles on average possess a larger inter-particle distance compared to the bulk particles. Further away, the longer-range attractive force vanishes, the virial pressure becomes less negative, and it eventually goes to zero when the average inter-particle distance is larger than r_c .

The sum of the conservative and thermal terms forms the overall pressure field according to Eq. (19) and is displayed in Fig. 2(c). The difference between the normal and the tangential component of the spherical interface is displayed in Fig. 2(d). For clarity, the diagrams from the smallest of the three droplets are omitted in this figure. The positive peak at the drop interface, followed by noise in the bulk (also omitted for clarity), illustrates the non-hydrostatic nature of the virial stress tensor that is responsible for surface tension. This diagram is consistent to what has been observed in molecular dynamics simulations for a Lennard-Jones fluid in a slab geometry.²¹

The surface tension coefficient can be calculated directly according to the Y-L relation from the slope of the lines fitting the values of ΔP at various diameters; see Fig. 3. It is noted that this is not the only methodology to evaluate σ and that a more complete discussion can be found, for instance, in Refs. 8 and 19. The radius of curvature of the drop is determined from the point where the number density falls below half of the bulk density value. This is a relatively precise measurement given the steepness of the interface at this temperature. The internal pressure is taken from the virial plateau value, with an uncertainty of ± 0.4 for the smallest droplets and of less than ± 0.002 for the largest drops in the range considered here. The MDPD parameters and the corresponding values of σ are listed in Table I. The values found for Sets 2 and 7 are in close agreement with the values reported in Ref. 13 (4.95 and 7.54) for the same parameters. The properties from Table I will be used in Sec. III A to characterize the sensitivity of surface tension to the MDPD parameters.

A. Surface tension parameters

It is important to determine whether MDPD can generate number density and surface tension values that are consistent with the properties of real liquids. We begin by plotting ρ and σ from Table I together with the corresponding properties of common liquids at ambient conditions (from Ref. 22): ether; acetone; methanol; benzene; water; and glycerol. In Fig. 4, the MDPD density and surface tension calculated for Set 2 are converted to match the properties of ether. This choice is arbitrary but convenient in grouping the properties of the MDPD fluids from Table I within the same range of ρ and σ from real liquids. The plot illustrates how relatively small variations of the interaction parameters can produce substantial change of properties.

The behavior of σ can be related more precisely to the interaction potential by taking a virial approach. The exact virial formulation of the surface tension coefficient is based on the density correlation across the liquid-vapor interface, which is difficult to determine. A simplification, first introduced by Fowler,²³ consists in substituting the density pair

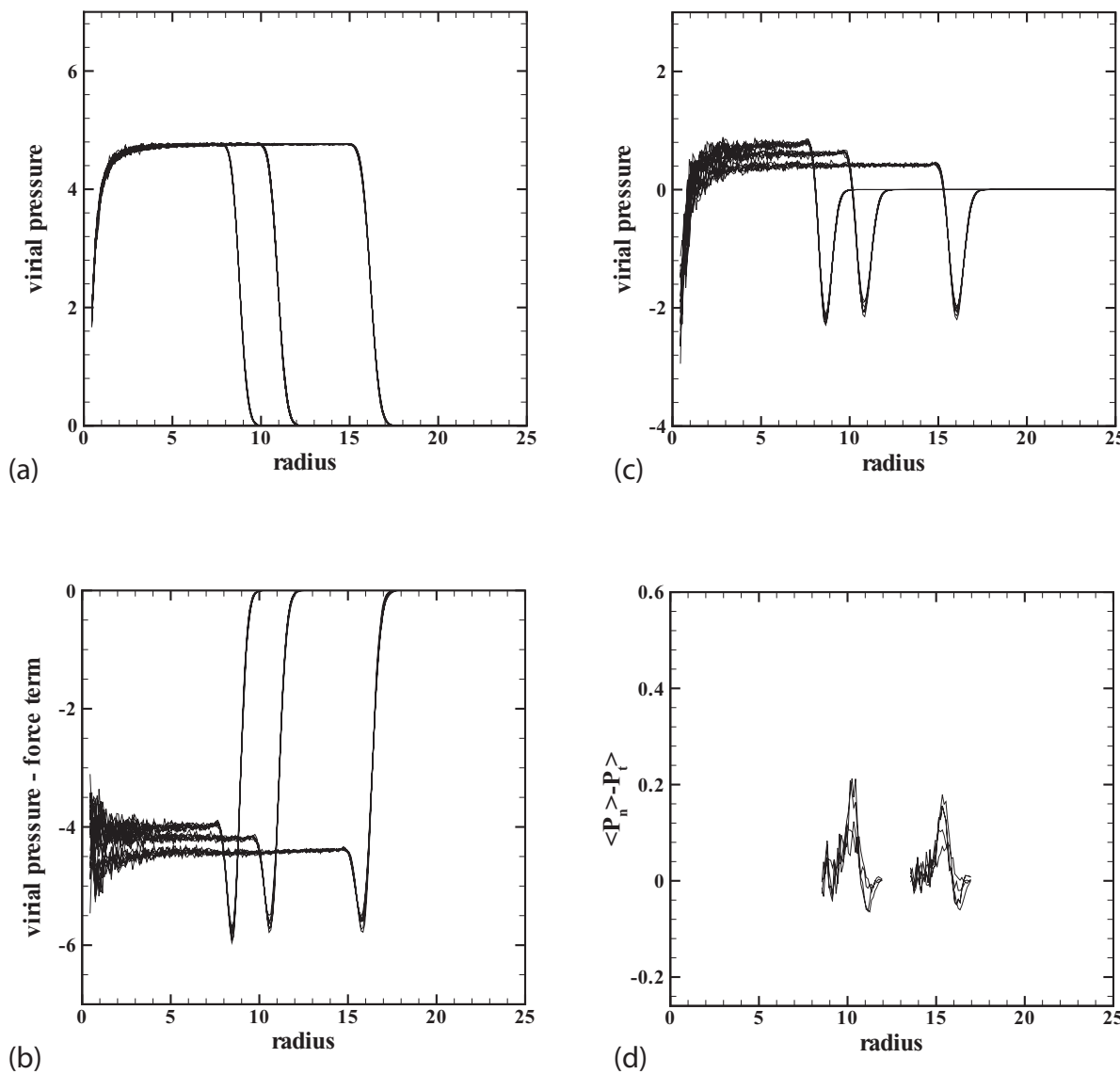


FIG. 2. Virial pressure as a function of radius for three drops of fluid 1 (the interaction parameters are listed in Table I): (a) contribution of thermal motion [first term in Eq. (19)]; (b) contribution of the conservative forces [second term in Eq. (19)]; (c) resulting virial pressure; (d) radial minus tangential component of virial pressure.

correlation at the interface with the product of the bulk liquid density and the radial distribution function $g(r)$. This yields an approximate mean-field expression for a given potential $u(r)$,

$$\sigma^{MF} = \frac{\rho^2}{8} \int_0^\infty dr r^4 u'(r) g(r), \quad (20)$$

that only requires a model for $g(r)$.

The no-interaction model of a dilute gas, $g(r) \simeq 1$, obviously does not apply to the liquids studied here, but provides a first idea of the functional dependence of surface tension from the number density:

$$\sigma_{g(r)=1}^{MF} = -\frac{\pi}{240} (A r_c^5 \rho^2 + B r_d^5 \rho^3). \quad (21)$$

This equation shows that the effect on σ of varying A is separated from the effect of the other two parameters, which are lumped together in the product $B r_d^5$. The latter term highlights

the higher sensitivity of the fluid properties to the repulsive force cutoff r_d compared to the force amplitude B .

Empirical coefficients can be used to account for the “non-ideality” of the MDPD fluid, similar to what is done to derive the pressure-density relation.¹³ From linear fitting of the values in Table I, we find

$$\sigma^{fit} = -\frac{\pi}{240} (0.42 A r_c^5 \rho^2 + 0.0030 B r_d^5 \rho^3). \quad (22)$$

The values of σ^{fit} are listed on the last column of Table I for comparison with the coefficients calculated from the Y-L relation in Sec. III. With the exception of the two lowest values of surface tension coefficient, the difference is of the order of 20% or less.

The principal information that can be derived from Eq. (22) is that the highest-order dependence of the number density from the surface tension coefficient is cubic. In real liquids, the dependence of σ on density is of even higher order, as suggested by the almost universal relation $M^* \sigma^{1/4}$

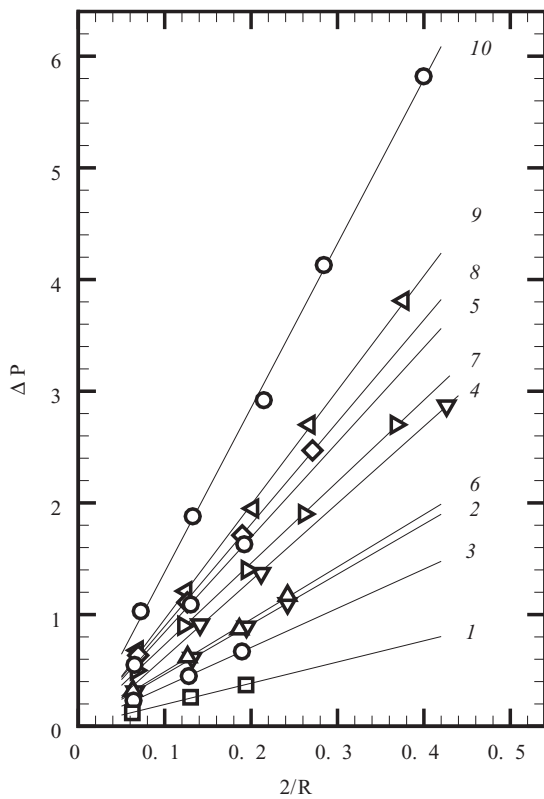


FIG. 3. Pressure difference across the liquid-vapor interface of a drop in equilibrium versus its curvature for the 10 MDPD fluids listed in Table I.

$= P(\rho_L - \rho_V)$,²⁴ where M^* is the molecular weight of the liquid and P is called the parachor.

The coefficients of σ^{fit} could be refined by carrying out the evaluation of surface tension in a more systematic manner. One can also consider a more realistic approximation of the radial distribution function in the form

$$g(r) = e^{-u(r)/kT}, \quad (23)$$

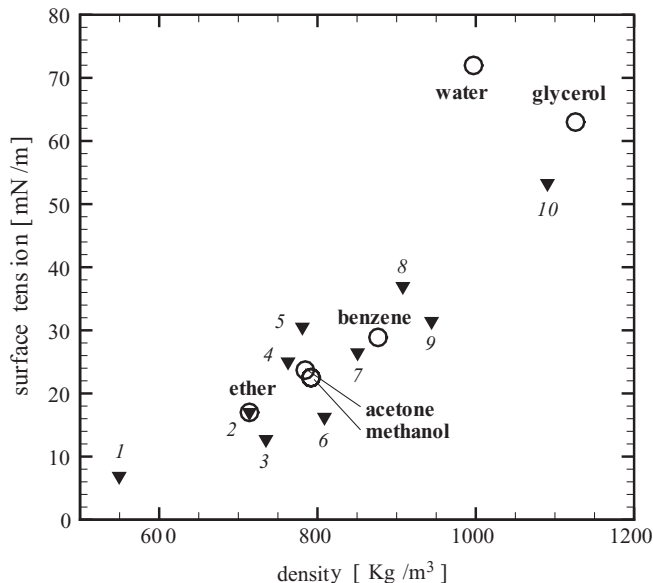


FIG. 4. Surface tension coefficient versus density for the MDPD fluids in Table I and for a group of real liquids at room temperature.

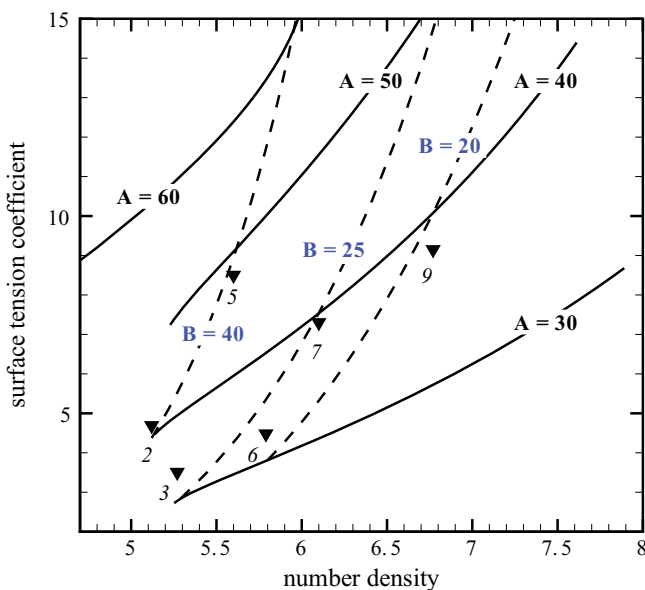


FIG. 5. Surface tension coefficient versus number density. The symbols are the calculated values from columns five and six in Table I; the continuous and dashed lines are plotted using Eq. (24) at constant A and B , in this order.

where the interaction potential $u(r)$ can be obtained by numerical integration of F_c with the condition $u(r_c) = 0$. The integral resulting from this expression,

$$\sigma^{MF} = -\frac{\rho^2}{8} \int_0^1 dr r^4 F_c(r) e^{u(r)/kT}, \quad (24)$$

has to be carefully evaluated, since, as noted by Lekner and Henderson,²⁵ there is a large degree of cancellation between positive and negative parts of the integrand. We find that, in line with Fowler's simplification, Eq. (24) is more accurate if the number density appearing in F_c is the bulk value ρ .

An example of the application of Eq. (24) is given in Fig. 5, where continuous lines are drawn at constant A by varying the parameter B . The repulsive cutoff is the same ($r_d = 0.75$), and $k_b T$ is maintained near 1. In the proposed procedure, the bulk density is first evaluated at a few discrete values, B_1, B_2, \dots ; then, σ^{MF} is calculated by quadrature from Eq. (24) as a function of B_i . The dashed lines of Fig. 5 are similarly obtained by keeping B fixed while varying A . Six of the intersections of the two families of curves correspond to parameter entries in Table I; the MDPD values of σ are plotted as solid symbols. The closeness of the symbols to the line intersections provides a sense of the accuracy of σ^{MF} . One can see that the correct trend is captured, and that the suggested estimate can guide the modeler in choosing the MDPD parameters to match a given surface tension coefficient.

Even without providing a closed-form solution, Eq. (24) can be used to explore the variation of σ within the parameter space of the interaction coefficients in a simpler way than by repeating evaluations of the Y-L relation. In fact, this mean field approximation does not require calibration or fitting, but only an estimate of ρ . More rigorous expressions for the surface tension coefficient are found in Ref. 25 for an assumed variation of the number density along the interface. For instance, a closed-form solution can be derived if the upper and

lower tails of the density profile are approximated by an exponential function. These expressions are however rather sensitive to the actual interface thickness and to the functional form of the density profile. We find that, in the absence of a verified model for the MDPD density profile, integral forms that are in principle more rigorous than Eq. (24) would be of limited usefulness, especially in view of the simple approximation used for $g(r)$.

B. Capillary pinch-off

The occurrence of capillary pinch-off has already been demonstrated by a modified DPD method²⁶ as well as by pioneering molecular dynamics simulations.²⁷ Here, we examine whether MDPD captures the correct fluid dynamic behavior by assessing the response of a quiescent circular jet of diameter D to a periodic axial perturbation. It is well known that the jet becomes unstable if $\lambda/D > \pi$.²⁸ Above that cutoff wavelength, the cylinder surface is driven toward the state with the smallest area, and, locally, to pinch-off. In this process, the greater the cohesion between the particles (and thus the surface tension), the faster the instability develops. Below the cutoff, surface tension has the opposite role of restoring the jet to its unperturbed state. In the inviscid description of the Plateau-Rayleigh instability,²⁹ linear analysis of perturbation leads to the maximum growth of a disturbance for $\lambda/D \simeq 4.5$. By dropping viscosity from dimensional analysis, the characteristic pinch-off time is

$$\tau = \sqrt{\rho D^3/\sigma}. \quad (25)$$

As a demonstration, simulations are carried out for two jet diameters in a 10^3 box with periodic boundary conditions and sinusoidal perturbation of wavelength $\lambda = 10$. The MDPD parameters correspond to Set 2 in Table I. The random and dissipation coefficients are $\xi = 12$ and $\gamma = 72$; the time step is $\Delta t = 0.001$.

In the first simulation, we set $L/D = 4.5$ with 251 particles. Figure 6(a) displays a sequence of snapshots as seen through a slice of the jet. Initially, the amplitude of the perturbation is only one layer of particles. The jet begins to neck at around $t = 2.7$ and pinches off soon thereafter, so that by $t = 13$ the two half droplets have fully equilibrated. The characteristic time from Eq. (25) is $\tau = 3.46$. The actual time to pinch-off depends on the seed values that are used to generate random numbers for the stochastic force and for the initial velocity distribution. It is, however, well defined in every realization of this case.

In the second simulation, the diameter is increased to $D = 5$, with 1116 particles. No capillary instability develops, even for large amplitude perturbations, and the jet returns to a cylindrical shape under the restoring force of surface tension. The simulation can continue for a very long time (the last frame of Fig. 6(b) shows a snapshot at $t = 200$) without pinch-off ever occurring. This and the previous result are consistent with the Plateau-Rayleigh analysis.

To verify that the simulations are converging according to Füchslin's scaling,¹⁸ Fig. 7 shows snapshots taken immediately after pinch-off for four distinct cases. Frame (a) cor-

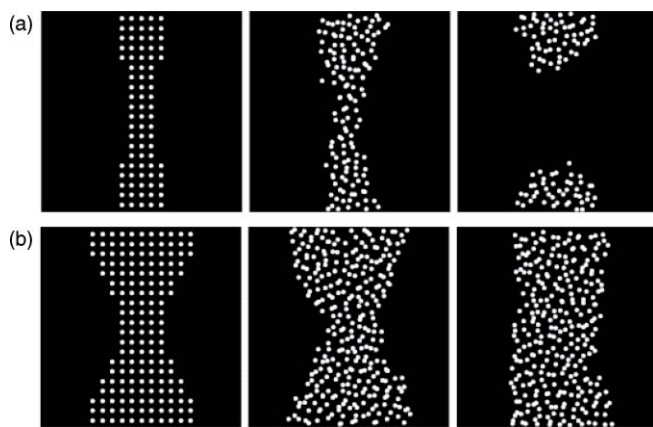


FIG. 6. Snapshots of capillary dynamics of a liquid thread: $L/D = 4.51$ (top) and $L/D = 2.5$ (bottom).

responds to the baseline with 251 particles. Frame (b) corresponds to a simulation with 2008 particles distributed within the same domain size. At $\phi = 1/8$, each particles carries 0.125 times the mass of a particle of the baseline and has a cutoff of $r_c = 0.5$. The remaining interaction parameters are similarly scaled according to Eqs. (13) and (17). The particle distribution is less rarefied compared to the baseline, compensating the fact that each particle generates shorter and weaker forces. The third and fourth frames in Fig. 7 correspond to a simulation with 16 064 particles ($\phi = 1/64$) and with 128 512 particles ($\phi = 1/512$), respectively. Interactions are even weaker and the shape near pinch-off is delineated more clearly than in the other two cases. Two thin liquid bridges can be observed while they rapidly retire toward the two half drops. The shape of the pinched thread can be said to be converged at $\phi = 1/64$ since there are minimal differences with the $\phi = 1/512$ calculation.

To establish a connection with the theory, the minimum thread radius h_{min} can be plotted as a function of the time to breakup, $t_0 - t$. Even if every MDPD simulation has its

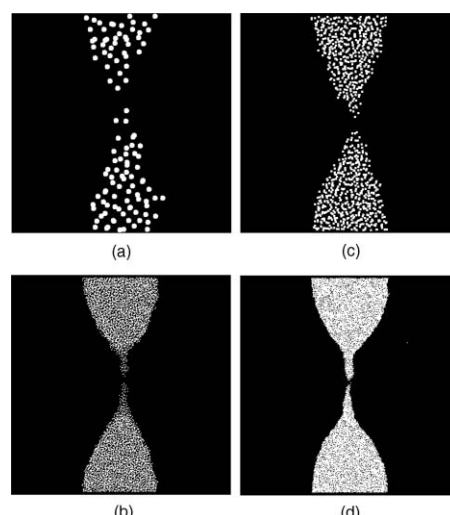


FIG. 7. Snapshots of a liquid thread immediately after pinch-off. A slice through the thread is shown for: (a) 251 MDPD particles; (b) 2008 particles; (c) 16 064 particles; and (d) 128 512 particles.

own specific trajectory, this plot is expected to follow a specific power law that depends on the Ohnesorge number, $\text{Oh} = \mu/\sqrt{d R \sigma}$, where μ is the dynamic viscosity and $R = D/2$. Analysis results of pinch-off dynamics are extensively reviewed by Eggers and Villermaux.³⁰ In the absence of an outer fluid, pinch-off proceeds according to a solution that balances surface tension, viscous, and inertial forces. For sufficiently small values of Oh , viscosity drops out of the description and $h_{\min} \sim (t_0 - t)^{2/3}$ [see also Eq. (25)]. Viscous effects become important as the minimum radius of the thread continues to decrease, and eventually the flow transitions to an inertial-viscous regime where $h_{\min} \sim t_0 - t$. On even smaller scales, it can be postulated that the driving force leading to pinch-off consists of thermal fluctuations at the molecular level. The relevant length scale in the shift from deterministic to stochastic emerges from the comparison of the thermal energy with the surface energy,

$$\ell_T = \sqrt{k_B T / \sigma}. \quad (26)$$

The domain concerned by thermal fluctuations (up to a few hundreds of nanometers) has been recently probed by MD. MD simulations of nanojets show a substantial change in behavior near pinch-off.³¹ This behavior is predicted by the stochastic lubrication equation (SLE),²⁷ derived from the Navier-Stokes equations in the limit of a slender jet and with the addition of Gaussian noise to the deterministic stress tensor. The relation between h_{\min} and $t_0 - t$ is described by a power law with exponent 0.418, found by numerical integration.³²

The logarithmic plot of $h_{\min}(t_0 - t)$ in Fig. 8 demonstrates that a single MDPD simulation can span the three scaling behaviors listed above. To track the minimum jet radius, it is necessary to post-process several snapshots of particle positions, each axially sliced into 50 bins. It is assumed that the only 1% or less of the particles lie outside the surface of the jet, a threshold consistent with almost no vapor phase. The jet radius, calculated with respect to the instantaneous position of the center of mass in each slice, is defined based on the radial histogram of number density. The pinch-off time is established as the instant when one of the bins becomes empty. The simulation is carried out in a 80^3 periodic cube using the parameter set 7 from Table I for a system of 118 657 particles; the time step is $\Delta t = 0.001$. The dissipation and random coefficients are $\gamma = 0.5$ and $\xi = 1$, giving $v = 0.072$; the Ohnesorge number is therefore $\text{Oh} = 0.022$.

The time to pinch-off in Fig. 8 is normalized by τ , whereas h_{\min} is normalized by the unperturbed jet radius R . Initially, and for almost a time decade, the tracked points are aligned along the 2/3 slope. The inertial-viscous behavior appears at approximately $h_{\min} = 0.3 R$ and is quickly overtaken by a trend where most of the points align along the slope 0.418. This occurs approximately at $h_{\min} = 0.15 R$, above the thermal capillary length $\ell_T = 0.042 R$. At that point, as noted by Eggers,³² any random fluctuation which increases the thread radius will also increase its effective mass, slowing down the motion of the fluid; conversely, any fluctuation toward a smaller neck radius will accelerate pinch-off. The gap between deterministic hydrodynamics and molecular dynamics is thus bridged in this simple example. Other

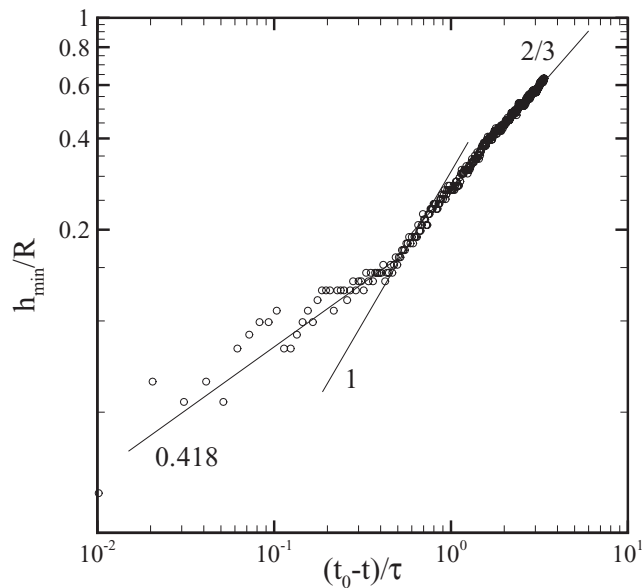


FIG. 8. Variation of minimum thread radius h_{\min} versus time to breakup $t_0 - t$. The three lines correspond to potential flow (slope 2/3), inertial-viscous (slope 1), and stochastic (slope 0.418) power laws. The open symbols are measured values from the MDPD simulation.

MDPD simulations (not shown here) confirm that a larger viscosity or a smaller domain causes the potential-flow scaling to disappear from the diagram.

IV. WALL WETTING MODEL

In the last part of this work we show how different hydrophobic or hydrophilic wetting behaviors can be reproduced by tuning the magnitude and/or the range of additional repulsive and attractive forces generated by a solid interface. We follow the approach of previous studies,^{33,34} where the wall-fluid interaction was modeled by combining attractive and repulsive forces from the bell-shaped weight function of smoothed particle hydrodynamics (SPH),

$$F_{sl}^c(r) = A^S w_c^S(r, r_c^S) + B^S w_d^S(r, r_d^S). \quad (27)$$

The parameters A^S and B^S determine the relative strengths of the attractive and repulsive interactions. The shape functions $w^S(r, r^S)$ are non-normalized cubic splines with cutoff length r^S . A similar combination of SPH shape functions was used by Liu *et al.*³³ to model inter-particle interactions in their modified DPD approach. However, since the SPH shape function vanishes at the origin (see the dashed curve in Fig. 9), no repulsive forces in response to overlapping particles can be generated near the wall. At high pressure, this feature tends to form dense clusters with several particles per site. This behavior can be corrected by keeping a constant nonzero value of F_{sl}^c near the origin as shown in Fig. 9. This “anti-clustering” SPH kernel³⁵ is used in all the following examples, where we retain the MDPD interactions to calculate inter-particle forces. We will show that hydrophobic and hydrophilic behaviors can be generated depending on the selection of $A^S \leq 0$, $r_c^S, B^S > 0$ and r_d^S .

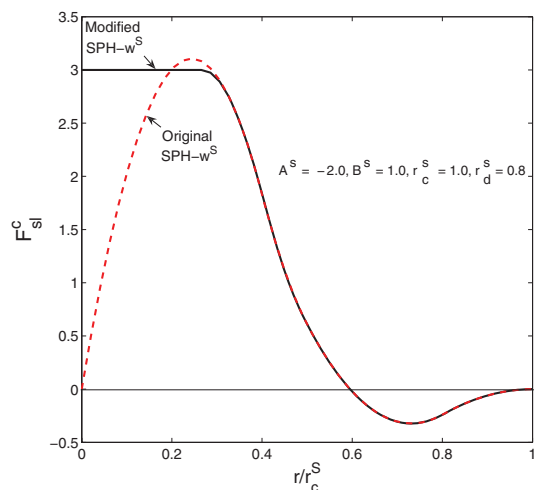


FIG. 9. The liquid-solid interaction defined by the modified SPH weight function (solid line), compared with the original SPH weight function (dashed line) used in Refs. 33 and 34.

A. Contact angles and slip lengths

We start by showing that the contact angles resulting from particle-wall interactions in channel flow simulations are consistent with the previously calculated values of σ from drops in equilibrium. Flow in a channel is simulated by adopting the strategy proposed by Liu *et al.*³⁴ Particles are initially positioned at random in the computational domain with the number density of the fluid. The system is then run to equilibrium using repulsive particle-particle interactions only. The particles within a certain range (of order r_c^S) from the wall surface are frozen to represent the solid grains. The inflow is simulated by injecting particles into the channel near the inlet with velocities specified by the Maxwell distribution at the specified inlet temperature; the particles are injected at time intervals of 0.01. The outflow is produced by deleting the particles at the outlet.

After the system is run to equilibrium, the free-surface of the liquid forms a well-defined contact angle θ with respect to the solid surface. The liquid-vapor interface is fitted by a 4th order polynomial to determine the contact angle from the slope of the polynomial at the wall. The curvature is related to θ and to the capillary width $2a$ by the relation $R = a/\cos\theta$, where R is the principal radius of the interface curvature. In a two-dimensional capillary channel, the Y-L relation can be simplified as $\Delta P = \sigma/R$ and the pressure difference is

$$\Delta P = \frac{\sigma \cos \theta}{a}. \quad (28)$$

The points in Fig. 10 are obtained from Eq. (28) using a set of simulations where the value of A^S is varied from 0.0 to -80 with fixed $B^S = 20$, $r_d^S = 0.7$, and $r_c^S = 0.8$. The MDPD fluid is specified by Set 8 from Table I. From the linear fitting of ΔP versus $\cos\theta/a$, the surface tension coefficient is 10.84, which is close to the value 10.2 found in Sec. III.

Decreasing the absolute value of A^S corresponds to changing the properties of the wall, and effectively shifts the behavior of the fluid from hydrophilic to hydrophobic. Examples of hydrophilic (wetting) and hydrophobic (non-wetting)

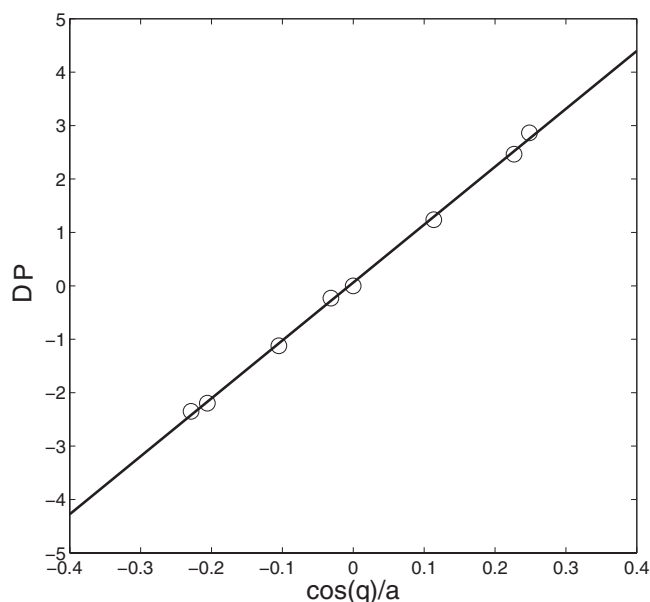


FIG. 10. Pressure difference across the liquid-vapor interface (ΔP) versus the cosine of contact angle ($\cos\theta$). The surface tension coefficient from the linear fit is $\sigma = 10.84$.

behaviors are illustrated in Fig. 11 (top and bottom frame, respectively) with $A^S = -10$ and $A^S = -60$.

In the hydrophilic flow, the fluid tends to spread near the wall and, as shown by the density profile of Fig. 12, this spreading is accompanied by density fluctuations. Density fluctuations are attenuated in hydrophobic flow, since the liquid is more uniformly dispersed. They can also be reduced, as proposed by Henrich *et al.*,³⁶ by letting the wall and the fluid particles mix together while keeping distinct the two parameter sets. This solution is not completely satisfactory, since it causes the liquid-solid interface to become fuzzy. We attempted to solve this problem by exerting extra normal forces on fluid particles near the wall, but this approach failed because it disturbed the liquid-solid interaction and altered the wetting behavior. A more in depth study of the wetting mech-

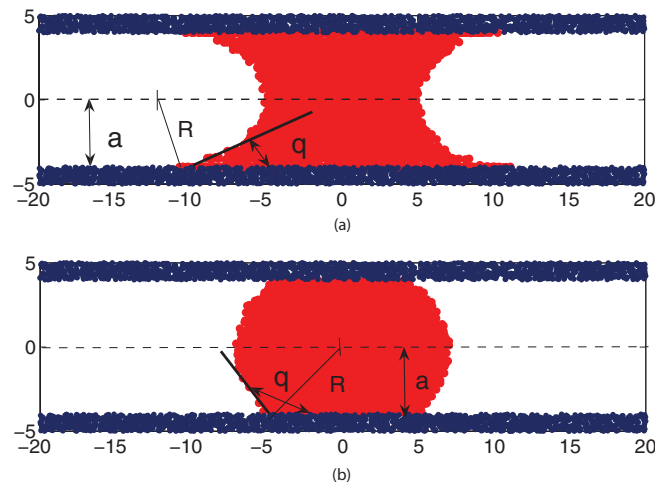


FIG. 11. Static contact angle of a MDPD fluid in contact with different solid surfaces: hydrophilic (top); hydrophobic (bottom).

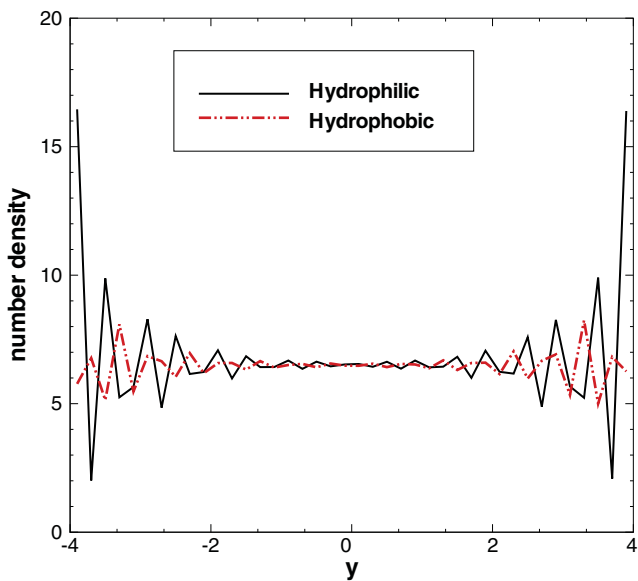


FIG. 12. Number density distribution of fluid particles across the channel.

anism is required, perhaps through simulations at the molecular level, but it is not attempted here.

In the hydrophobic flow, the velocity profile of Fig. 13 suggests the existence of slip. To quantify slip, the fully developed velocity profile is fitted by a Poiseuille parabola (solid line) with no-slip at the wall. The slip length L_s is then evaluated from the distance L between the two points where the extrapolated Poiseuille parabola of the velocity profile vanishes,

$$L_s = L/2 - a. \quad (29)$$

The results for the parameters specified above are summarized in Fig. 14. The constancy of L_s with respect to the flow rate indicates that the liquid-solid interface leads to a Navier-type

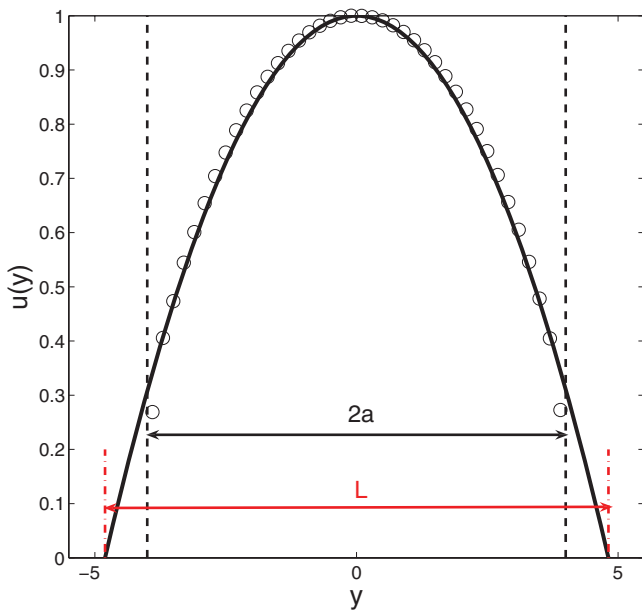
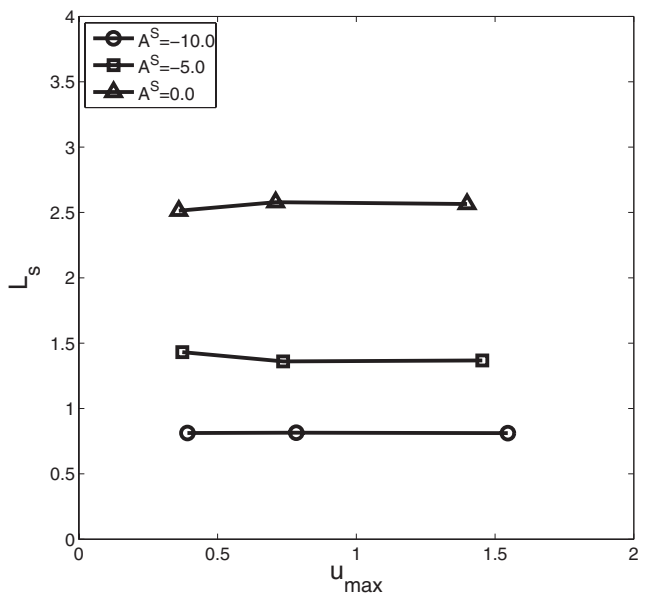


FIG. 13. Normalized velocity profile for a non-wetting MDPD fluid in a Poiseuille flow. The position of the wall is marked by dashed lines.

FIG. 14. Wetting-dependent slip length (L_s) as a function of the flow velocity. Here, u_{max} is the flow velocity at the channel center.

slip mechanism. L_s increases when the absolute value of A^S decreases, i.e., with increasing hydrophobicity of the solid. This tendency was also found in MD simulations of Lennard-Jones liquids.³⁷

B. Droplets through fracture junction

We now examine the dynamics of droplets entering an inverted Y-shaped fracture junction. It is known from experiments³⁸ that the behavior of droplets through the junction falls into three categories depending on the droplet length. Tartakovsky and Meakin³⁹ used SPH to reproduce these behaviors. In their simulations, the magnitude of the gravitational acceleration was changed instead of the droplet length to achieve a similar effect in terms of the Bond number,

$$Bo = d g L_1 L_2 / (2 \pi r_c^3), \quad (30)$$

where d is the fluid density, L_1 is the width of the fracture, L_2 is the droplet length, and g is the gravitational acceleration.

In our simulations, both the droplet length and the gravitational acceleration are changed; the results are shown in Figs. 15 and 16, respectively. The wall-fluid interaction is defined according to the following parameters: $A^S = -40$, $B^S = 20$, $r_d^S = 0.7$, $r_c^S = 0.8$, $L_1 = 4$. The fluid is specified by Set 8 from Table I. The three categories of droplet behaviors through an inverted Y-shaped fracture junction are described next.

The first category is “transition from droplet to film mode,” as named by Dragila and Weisbrod,³⁸ and was observed for small droplets (small L_2). The droplet cannot overcome the capillary barrier and stops at the junction without saturation. A concave meniscus is formed and a film flow along the upper wall of both fracture branches is developed. This is shown both in Fig. 15(a) for a smaller droplet ($L_2 = 8$, $g = 0.1$, $Bo = 1.922$) and in Fig. 16(a) for a smaller gravitational acceleration ($L_2 = 16$, $g = 0.05$, $Bo = 1.971$).

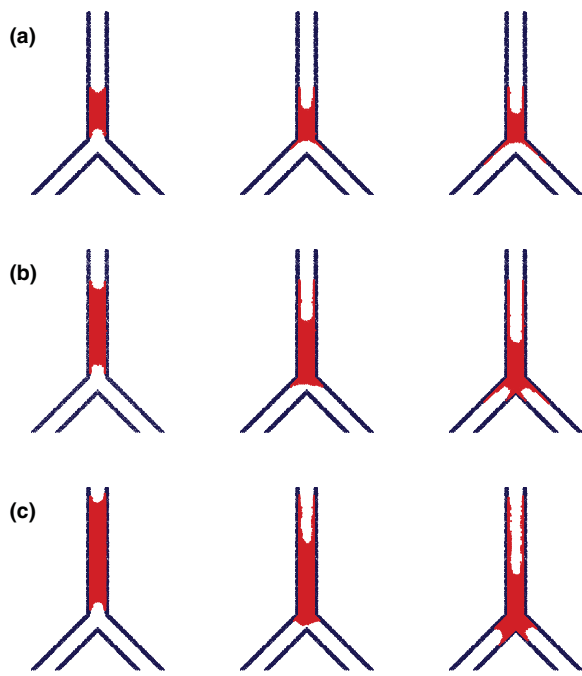


FIG. 15. The dynamics of droplets entering an inverted Y-shaped fracture junction as a function of the droplet size.

The second category, “droplets that saturated the intersection with a film precursor,” was observed for medium-size droplets.³⁸ The film flow still occurred in the experiment, but eventually saturated the junction. This behavior is also captured in our simulations by increasing either the droplet length [Fig. 15(b)] or the gravitational acceleration [Fig. 16(b)] with $L_2 = 16$, $g = 0.077$, and $Bo = 2.960$.

The last category is “droplets that saturated the intersection” for larger droplets:³⁸ the droplet was able to overcome

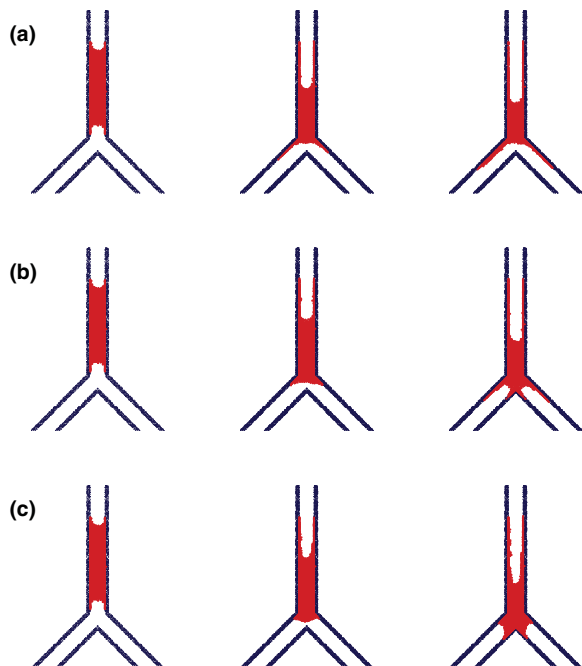


FIG. 16. The dynamics of droplets entering an inverted Y-shaped fracture junction as a function of the gravitational acceleration.

the capillary barrier rapidly and fully saturated the intersection without film flow developed. We further increased the droplet size or the gravitational acceleration to observe this behavior [Fig. 15(c) with $L_2 = 22$, $g = 0.1$, $Bo = 5.285$; and Fig. 16(c) with $L_2 = 16$, $g = 0.15$, $Bo = 5.913$].

Thus, MDPD simulations that include the proposed wall interaction model can capture all the essential elements of the experimental results.³⁸ According to the estimation by Tartakovsky *et al.*,³⁹ the Bond numbers corresponding to each category of experimental observations were $Bo < 2.059$; $2.059 < Bo < 3.089$; and $Bo > 3.089$, respectively. The Bond numbers calculated in our simulations fall into each range properly.

V. CONCLUSIONS

The mesoscale spatial and temporal scales (within 10 and 1000 nm, and within 1 ns and 10 ms) that are captured by coarse-graining particle techniques can significantly extend the reach of MD simulations while keeping the fundamental viewpoint that fluid properties arise from elementary particle interactions.

A specific feature of MDPD is that the potential energy is locally dependent on number density, so that a realistic dependence of the surface tension coefficient from ρ is built directly into the system. This point is illustrated in this paper by a direct comparison with the properties of liquids that are commonly used in applications. It is shown how, for a given level of coarse-graining, matching the surface tension coefficient, the density, and the kinematic viscosity of a given liquid with the properties of a system of MDPD particles determines all the interaction parameters. A numerical procedure is also devised that provides an approximation of σ from the quadrature of a function of the interaction potential. This procedure provides a simple tool to explore the parameter space of MDPD fluids in terms of their physical properties.

The MDPD scheme provides a viable mesoscale description of free-surface flow. This is shown in simulations where the dynamics leading to the pinch-off of a periodically perturbed liquid thread is correctly captured. Particularly, the principle of minimum surface energy as the criterion leading to pinch-off is naturally respected in the simulation. This result can be made independent from the particular coarse-graining chosen in determining the MDPD parameters, as proved by a scaling process where the number of molecules per particle is decreased (or increased) while the interaction forces become correspondingly more distributed (or more concentrated).

We also provide an example of pinch-off dynamics where the three power laws predicted by asymptotic analysis – potential flow, inertial-viscous, and stochastic – are captured. For a continuum flow discretization, the second transition is very difficult to reach because it occurs in the sub-micron range for most liquids. Conversely, molecular dynamics simulations are restricted to the stochastic regime because of the very small size of the computational domain they can interrogate. A domain sufficiently large to include the inertial regime can be obtained instead within the MDPD framework: the 80^3 simulation presented in this paper could be

completed in about five hours on an Intel® Xeon® Processor E5420.

The MDPD method is also well positioned for calculating wetting in microchannels. Near a solid wall, an “anti-clustering” SPH kernel is shown to generate a combination of short-ranged repulsion and long-ranged attraction between solid and fluid particles while avoiding spurious particle clustering near the wall. In combination with the MDPD interaction between liquid and vapor, this approach produces wetting and non-wetting behaviors, albeit with the undesirable density oscillations near the wall that seem to be common to particle-wall interactions. In one example of hydrophobic behavior, the slip length of a non-wetting flow is calculated as a function of the wall interaction parameters. Finally, in simulations of a droplet wetting an inverted Y-shaped microchannel junction, the essential dynamics observed in experiments is captured – namely, transition from droplet to film, saturation with film precursor, and saturation – for increasing values of the Bond number.

In closing, we note that since the random and dissipative forces of MDPD are in common with DPD, particles from the two schemes can be easily combined. The availability of both schemes in the same simulation would enable simulations of complex fluids with suspended particles, of bluff bodies in capillary networks, or of porous media dominated by capillary and shear forces, to name a few. These applications will be examined in future work.

ACKNOWLEDGMENTS

Support from the AFOSR contract AFD-070820-034 under the supervision of Dr. Fariba Fahroo is gratefully acknowledged. Also, G.E.K. would like to acknowledge partial support by the NSF CBET program.

- ¹H. Lei, B. Caswell, and G. E. Karniadakis, *Phys. Rev. E* **81**, 026704 (2010).
²P. V. Coveney and K. E. Novik, *Phys. Rev. E* **54**, 5134 (1996).
³S. I. Jury, P. Bladon, S. Krishna, and M. E. Cates, *Phys. Rev. E* **59**, R2535 (1999).

- ⁴K. E. Novik and P. V. Coveney, *Phys. Rev. E* **61**, 435 (2000).
⁵A. T. Clark, M. Lal, J. N. Ruddock, and P. B. Warren, *Langmuir* **16**, 6342 (2000).
⁶J. L. Jones, M. Lal, J. N. Ruddock, and N. Spenley, *Faraday Discuss.* **112**, 129 (1999).
⁷A. A. Louis, P. G. Bolhuis, and J. P. Hansen, *Phys. Rev. E* **62**, 7961 (2000).
⁸A. Tiwari and J. Abraham, *Phys. Rev. E* **74**, 056701 (2006).
⁹I. Pagonabarraga and D. Frenkel, *J. Chem. Phys.* **115**, 5015 (2001).
¹⁰S. Nugent and H. A. Posch, *Phys. Rev. E* **62**, 4968 (2000).
¹¹P. Españo and M. Revenga, *Phys. Rev. E* **67**, 026705 (2003).
¹²P. Españo, M. Serrano, and H. C. Ottinger, *Phys. Rev. Lett.* **83**, 4542 (1999).
¹³P. B. Warren, *Phys. Rev. E* **68**, 066702 (2003).
¹⁴S. Y. Trofimov, E. L. F. Nies, and M. A. J. Michels, *J. Chem. Phys.* **123**, 144102 (2005).
¹⁵S. J. Plimpton, *J. Comput. Phys.* **117**, 1 (1995).
¹⁶R. D. Groot and P. B. Warren, *J. Chem. Phys.* **107**(11), 4423 (1997).
¹⁷C. A. Marsh, G. Backx, and M. H. Ernst, *Europhys. Lett.* **38**, 411415 (1997).
¹⁸R. M. Füchsli, H. Fellerman, A. Eriksson, and H.-J. Ziock, *J. Chem. Phys.* **130**, 214102 (2009).
¹⁹A. Ghoufi and P. Malfreyt, *Phys. Rev. E* **82**, 016706 (2010).
²⁰M. Matsumoto and K. Tanaka, *Fluid Dyn. Res.* **40**, 546 (2008).
²¹A. Trokhymchuk and J. Alejandre, *J. Chem. Phys.* **111**, 8510 (1999).
²²J. A. Dean, *Lange's Handbook of Chemistry*, 18th ed. (McGraw-Hill Professional, New York, 1998).
²³R. H. Fowler, *Proc. R. Soc. London, Ser. A* **159**, 229 (1937).
²⁴S. Sugden, *The Parachor and Valency*, 1st ed. (G. Routledge, London, 1930).
²⁵J. Lekner and J. R. Henderson, *Mol. Phys.* **34**, 333 (1977).
²⁶A. Tiwari and J. Abraham, *Microfluid. Nanofluid.* **4**(3), 227 (2008).
²⁷M. Moseler and U. Landman, *Science* **289**, 1165 (2000).
²⁸J. A. F. Plateau, *Statique expérimentale et théorique des liquides soumis aux seules forces moléculaires* (Gauthier-Villars, Paris, 1873), Vol. 2.
²⁹J. W. S. Rayleigh, *Proc. R. Soc.* **29**, 7197 (1879).
³⁰J. Eggers and E. Villermaux, *Rep. Prog. Phys.* **71**, 036601 (2008).
³¹W. Kang, “Molecular dynamics simulations and microscopic hydrodynamics of nanoscale liquid structures,” Ph.D. dissertation (Georgia Institute of Technology, 2008).
³²J. Eggers, *Phys. Rev. Lett.* **89**, 084502 (2002).
³³M. B. Liu, P. Meakin, and H. Huang, *Phys. Fluids* **18**, 017101 (2006).
³⁴M. B. Liu, P. Meakin, and H. Huang, *Phys. Fluids* **19**, 033302 (2007).
³⁵P. A. Thomas and H. M. P. Couchman, *Mon. Not. R. Astron. Soc.* **257**, 11 (1992).
³⁶B. Henrich, C. Cupelli, M. Moseler, and M. Santer, *Europhys. Lett.* **80**, 60004 (2007).
³⁷P. A. Thompson and M. O. Robbins, *Phys. Rev. A* **41**, 6830 (1990).
³⁸M. I. Dragila and N. Weisbrod, *Water Resour. Res.* **40**, W02403 (2004).
³⁹A. Tartakovsky and P. Meakin, *Phys. Rev. E* **72**, 026301 (2005).